The Astrophysical Journal, 884:166 (7pp), 2019 October 20 https://doi.org/10.3847/1538-4357/ab3ec3

First Hard X-Ray Observation of a Compact Symmetric Object: A Broadband X-Ray Study of a Radio Galaxy OQ+208 with *NuSTAR* and *Chandra*

Małgosia Sobolewska[1], Aneta Siemiginowska[1], Matteo Guainazzi[2], Martin Hardcastle[3], Giulia Migliori[4], Luisa Ostorero[5], and Łukasz Stawarz[6]
[1] Harvard-Smithsonian Center for Astrophysics, 60 Garden Street, Cambridge, MA 02138, USA; msobolewska@cfa.harvard.edu
[2] European Space Research and Technology Centre (ESA/ESTEC), Kepleriaan 1, 2201 AZ, Noordwijk, The Netherlands
[3] School of Physics, Astronomy and Mathematics, University of Hertfordshire, College Lane, Hatfield AL10 9AB, UK
[4] INAF, Istituto di Radio Astronomia di Bologna, Via P. Gobetti 101, I-40129 Bologna, Italy
[5] Dipartimento di Fisica—Università degli Studi di Torino and Istituto Nazionale di Fisica Nucleare (INFN), Via P. Giuria 1, I-10125 Torino, Italy
[6] Astronomical Observatory, Jagiellonian University, ul. Orla 171, 30-244 Kraków, Poland
Received 2018 September 6; revised 2019 August 15; accepted 2019 August 23; published 2019 October 22

Abstract

Compact symmetric objects (CSOs) have been observed with *Chandra* and *XMM-Newton* to gain insights into the initial stages of a radio source evolution and to probe the black hole activity at the time of relativistic outflow formation. However, there have been no CSO observations to date at the hard X-ray energies (>10 keV), impeding our ability to robustly constrain the properties of the intrinsic X-ray emission and of the medium surrounding the young expanding jets. We present the first hard X-ray observation of a CSO performed with the *Nuclear Spectroscopic Telescope Array* (*NuSTAR*). Our target, OQ +208, is detected up to 30 keV, and thus we establish CSOs as a new class of the *NuSTAR* sources. We analyze the *NuSTAR* data jointly with our new *Chandra* and archival *XMM-Newton* data and find that a young (∼250 yr old) radio jet spanning the length of 10 pc coexists with cold obscuring matter, consistent with a dusty torus, with an equivalent hydrogen column density of $N_{\rm H} = 10^{23}$–10^{24} cm^{-2}. The primary X-ray emission is characterized by a photon index of $\Gamma \sim 1.45$ and an intrinsic 0.5–30 keV luminosity of $L \simeq 10^{43}$ erg s^{-1}. The results of our spectral modeling and broad-line optical classification of the source suggest a porous structure of the obscuring torus. Alternatively, the source may belong to the class of optically unobscured/X-ray-obscured active galactic nucleus. The observed X-ray emission is too weak compared to that predicted by the expanding radio lobes model, leaving an accretion disk corona or jets as the possible origins of the X-ray emission from this young radio galaxy.

Key words: galaxies: active – galaxies: evolution – galaxies: jets – X-rays: galaxies

1. Introduction

Theories of radio source evolution indicate that the initial expansion results in strong interactions between the radio outflow and the interstellar medium (ISM) within the central regions of the host galaxy. If the central regions are dense, then such interactions will generate strong shocks impacting the ISM and clearing out the path for a jet (Begelman & Cioffi 1989; Heinz et al. 1998; Wagner & Bicknell 2011). Additionally, models predict that this initial evolutionary phase is characterized by a high radio luminosity (Begelman & Cioffi 1989) and that the radio plasma contained in the compact lobes produces high-energy emission via the inverse Compton process (Stawarz et al. 2008; Migliori et al. 2014) or through strong shocks driven into the ISM by the expanding cocoon (Reynolds et al. 2001). However, there is little observational evidence to support these predictions as to date only one young radio source has been detected in the γ-ray band (Migliori et al. 2016). Furthermore, the quality of the X-ray data currently available for the young radio sources is still rather poor, as these sources are often faint and require long *Chandra* and *XMM-Newton* integration times to collect enough photons for a meaningful spectral analysis. Only a small number of compact symmetric objects (CSOs) have been studied in X-rays, yielding observed 2–10 keV fluxes of the order of 10^{-14}–10^{-13} erg cm^{-2} s^{-1}, and none at energies above 10 keV (Siemiginowska 2009; Siemiginowska et al. 2016, S16 hereafter).

Nevertheless, several CSOs have recent, good signal-to-noise X-ray spectra, allowing for detailed studies of their high-energy properties. Analyses revealed that these sources produce complex X-ray emission in which the primary power-law continuum, from either an accretion disk corona, jets, or expanding radio lobes, is modified by absorption and reflection processes (e.g., Guainazzi et al. 2004; Siemiginowska et al. 2008; Tengstrand et al. 2009; S16; Sobolewska et al. 2019).

In this paper, we present an X-ray study of OQ +208 (1404 +286), a nearby ($z = 0.0766$, Stanghellini et al. 1993) radio source classified as a CSO based on the properties of its radio morphology. The double radio structure, with two components separated by 10 pc; the symmetry of the radio source; and multi-epoch radio monitoring allowed kinematic age measurements that showed that the radio source is 255 ± 17 yr old (Wu et al. 2013). The source is located in a nearby disturbed galaxy, Mkn 668, that shows signs of a past merger (Stanghellini et al. 1993). Based on its optical spectrum, it is classified as a broad-line radio galaxy (Marziani et al. 1993). The archival *XMM-Newton* spectrum showed a steep soft X-ray component of an unknown origin and a hard highly absorbed X-ray continuum with a strong Fe–Kα emission line (Guainazzi et al. 2004). Thus, we observed the source with *Chandra* and with the *Nuclear Spectroscopic Telescope Array* (*NuSTAR*), in order to construct and model its broadband X-ray spectrum, to search for any extended X-ray emission, and to detect, for the first time, a young radio source above 10 keV.

Table 1
Log of X-Ray Observations of OQ +208

	Date	Mission	Instrument	ObsID	Exposure (s)	Total[a] Counts	Net[a] Counts
1	2014 Sep 4	*Chandra*	ACIS	16071	34604	678	650.0 ± 26.5
2	2016 Jun 18	*NuSTAR*	FPMA	60201043002	50354	756	553.6 ± 51.8
3	2016 Jun 18	*NuSTAR*	FPMB	60201043002	50150	704	484.4 ± 52.8

Note.
[a] Total and background subtracted counts in a circle centered on the source position: (1) *Chandra* with a 1.″5 radius and the energies between 0.5 and 7 keV, and (2) *NuSTAR* with a 49.″2 radius and the energies between 3 and 30 keV.

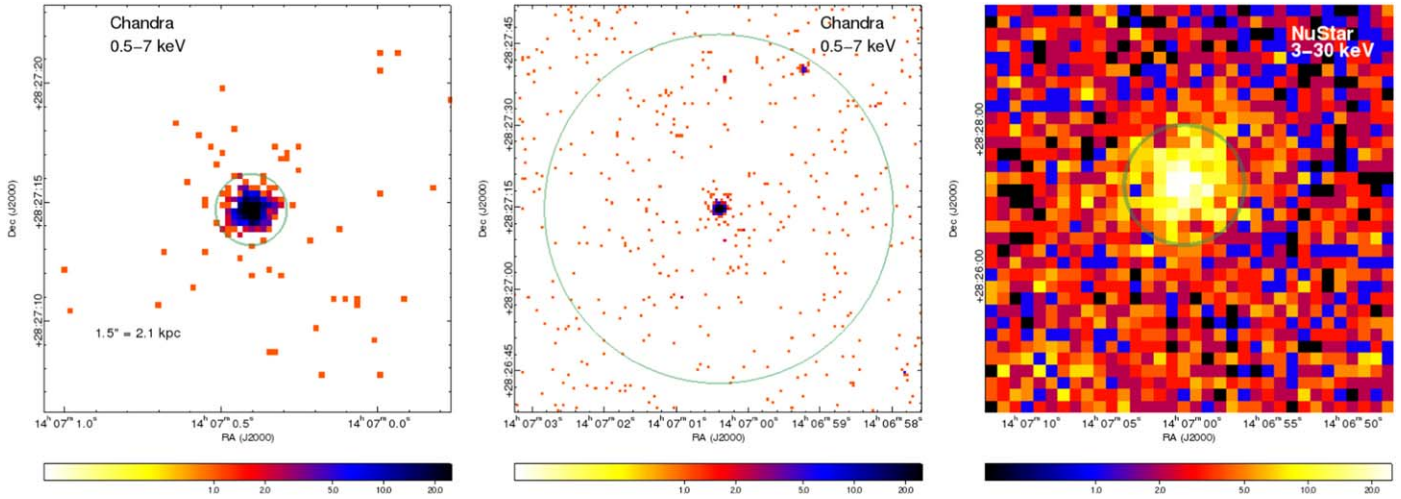

Figure 1. Left: *Chandra* ACIS-S image of OQ +208 in the 0.5–7 keV energy range, with the source region marked with the green circle with the radius of 1.″5 (corresponding to 2.1 kpc at the redshift of the source). The pixel size is 0.″249. Center: *Chandra* ACIS-S image binned to a pixel size of 0.″492 showing a larger view of the area with the *XMM-Newton* extraction region marked with the green circle with the radius of 32″. The secondary source at the ∼30″ distance is visible in the top right section of the image. Right: *NuSTAR* FPMA 3–30 keV image of OQ +208 with the 50″ radii circular region centered on the position of OQ +208 marked by the green circle. The *NuSTAR* image is binned by a factor of 4 with 1 pixel corresponding to ∼10″. The color log scale is marked on the bottom of each image indicating the number of counts in a pixel.

Our data allow us to disentangle the individual X-ray emission components and to obtain the energetics of the primary emission associated with this young radio source, as well as to study the properties of the environment in which the source is expanding. Our relatively deep *Chandra* observation shows no significant X-ray diffuse emission on the scales exceeding 3″, indicating that the complex emission arises from the central regions. The *NuSTAR* observation provides crucial constraints on the high-energy spectral properties by extending the available energy coverage over which the source is detected to ∼30 keV. In Section 2, we present our new *Chandra* and *NuSTAR* data and provide the details about the spectral model adopted in our analysis. In Section 3 we present our results, and we discuss them in Section 4. We summarize our findings in Section 5.

We use the most recent cosmological parameters (Hinshaw et al. 2013; $H_0 = 69.3\,\mathrm{km\,s^{-1}\,Mpc^{-1}}$ and $\Omega_m = 0.287$) implemented as WMAP9 in the `cosmology` package (Astropy Collaboration et al. 2018).

2. Data and Spectral Modeling

2.1. Chandra

OQ +208 was observed with *Chandra* ACIS-S for ∼30 ks (ObsID = 16071, see Table 1 for details). The target was placed at the aim point on the back-illuminated ACIS charge-coupled device (CCD, ACIS-S3). The observations were made in the VFAINT mode with a 1/8 CCD readout (*Chandra* Proposers Observatory Guide[7]). The target was clearly detected with *Chandra* (see Figure 1).

We used the *Chandra* CIAO software version 4.9 (Fruscione et al. 2006) and CALDB version 4.7.6 to process the data. We used the CIAO tool `acis-process-events` and applied the newest calibration files, filtered VFAINT background events, and ran a sub-pixel event-repositioning algorithm (and set `pix_adj=EDSER`). This final step provides the highest angular resolution X-ray image data for the most up-to-date ACIS-S calibration. Figure 1 displays the *Chandra* ACIS-S counts image in the 0.5–7 keV energy range, with the central 1.″5 (Section 2.1), kpc at the redshift of the source radius circle centered on the coordinates of OQ +208 (14:07:00.41, +28:27:14.65) marking the extraction region of the point-source emission. The entire X-ray emission is contained in this region with low background counts scattered over the entire image. For the background, we used an annular region centered on the same position, with inner and outer radii of 2″ and 5″.

On a larger scale, we detected a point X-ray source located 30″ (∼44 kpc at $z = 0.0766$) in the northeast direction from the OQ +208 center. Since the two radio lobes in OQ +208 extend along the northwest–southwest axis, it is not likely that this source could be associated with a hot spot or past radio activity of the source. There is no obvious optical counterpart to the

[7] http://cxc.harvard.edu/proposer/POG/

secondary source in the Sloan Digital Sky Survey. We note that the secondary, if persistent, would be included within the XMM-Newton EPIC-PN camera source extraction region in Guainazzi et al. (2004). However, in our *Chandra* data, we detect only 27 counts from this source, as opposed to 650 counts from the OQ +208 extraction region. Thus, we assess that the secondary source does not contribute significantly to the *XMM-Newton* spectrum of OQ +208.

2.2. NuSTAR

The *NuSTAR* (Harrison et al. 2013) observation of OQ +208 was performed on 2016 June 18 for about 51 ks (ID 60201043002) using two telescopes, FPMA and FPMB. We used HEAsoft 6.22.1 and `nustardas_06Jul17_v1.8.0` software with the CALDB version 20171002 for data processing. We run `nupipeline` and `nuproduct` to apply dead time correction, to account for SAA passages with `SAAMODE=optimize`, to apply new calibration, to extract spectra, and to generate appropriate response files. The source was clearly detected with *NuSTAR* (Figure 1). We assumed a circle with the default 49.″2 radius centered on OQ +208 coordinates (14:07:00.4, +28:27:14.6) for extracting the source spectra. For the background, we used annular regions centered on the same position with inner and outer radii of 123″ and 196″, respectively. Table 1 shows the resulting exposure and the number of counts for each telescope.

2.3. Spectral Modeling

Guainazzi et al. (2004) observed OQ +208 with *XMM-Newton* and inferred that it could be a Compton thick active galactic nucleus (AGN) based on its apparently hard photon index and a strong neutral iron line emission. However, *XMM-Newton* data alone were not sufficient to constrain the photon index of the source and the amount of the intrinsic absorption. Here, we model simultaneously the new *Chandra* and *NuSTAR* data, as well as the archival *XMM-Newton* PN data of OQ +208 using the `XSPEC` 12.9.1 software package with C-stat statistic (Arnaud 1996). We allow for cross-normalization constants between the four data sets.

We construct a model in which the intrinsic X-ray emission of the source is described with a power-law function with a photon index, Γ, and an exponential cutoff fixed at $E_{\rm cut} = 300$ keV, absorbed by the Galactic and host galaxy hydrogen column densities ($N_{\rm H}^{\rm gal}$ and $N_{\rm H,1}$, respectively). The X-ray emission above ∼4 keV contains a strong contribution from the reflection of the primary X-ray continuum from a cold matter, presumably a toroidal structure around the central black hole, which we describe with the torus model of Baloković et al. (2018). The level of the soft X-ray emission below 4 keV requires that we include the scattered intrinsic continuum in the model. The complete model can be written as: $A_{\rm instr} \times M_{\rm abs,1} \times [C_{\rm scat} \times$ `cutoffpl` + - $M_{\rm abs,2} \times$ `cutoffpl` + `torus`], where $A_{\rm instr}$ stands for a constant introduced in order to account for the uncertainties in the cross-normalization of the data sets from the different telescopes; $M_{\rm abs,1} = \exp(-N_{\rm H}^{\rm gal}\sigma_E)\exp(-N_{\rm H,1}\sigma_{E(1+z)})$ where σ_E is the photoelectric cross-section (in practice, $M_{\rm abs,1}$ equals `phabs * zphabs` in the `XSPEC` nomenclature); $M_{\rm abs,2} = \exp[-N_{\rm H,2}(\theta)\sigma_{E(1+z)}]$ is the zeroth-order multiplicative table given by Yaqoob (2012) and it accounts for the angle dependent absorption of the primary continuum by the obscuring torus; and $C_{\rm scat}$ is the normalization constant corresponding to the scattered power-law emission. The torus component is described using the table models provided by Baloković et al. (2018). They self-consistently compute the reflection continuum and fluorescent Kα_1, Kα_2, and Kβ emission lines for atomic species up to zinc. Here, `torus` = `ref_cont` + $C_{\rm line} \times$ `lines`, where we introduce a normalization constant $C_{\rm line}$ to account for the deviations from the perfect torroidal geometry. We investigate two scenarios: one where the line-of-sight column density, $N_{\rm H,2}$, and the average torus column density, $N_{\rm H}^{\rm torus}$, are linked to each other; and one where they are allowed to vary independently (corresponding to a porous torus case).

Stanghellini et al. (1997) reported that the milliarcsecond morphology of the radio emission in OQ +208 shows a flux density ratio between the two components of about 10:1. Based on the optical image of the galaxy, they indicate that the jet inclination of ∼45° is possible if the radio axis is aligned with the optical axis. They argue that the bulk velocity of ∼0.5c for this inclination angle could explain this flux density ratio via Doppler boosting. However, they also point out that the difference in the flux density may simply reflect random differences between the paths of the jets. Here, we assume that the radio jet is oriented in the plane of the sky (perpendicular to our line of sight), and the torus is perpendicular to the jet axis. Thus, we fix the inclination angle at a value corresponding to the ∼84°–90° in the torus model of Baloković et al. (2018).

3. Results

3.1. The First Detection of Hard X-Ray Emission from a Compact Symmetric Object

Our *NuSTAR* observation of OQ +208 provides the first hard X-ray (>10 keV) detection of a CSO and establishes these young radio sources as a new class of hard X-ray emitters. The source is detected up to 30 keV, at the 6σ confidence level within the 10–30 keV energy band.

3.2. Broadband X-Ray Spectrum of OQ +208

We found that the spectral model described in Section 2.3 fits well our broadband multi-instrument X-ray data. Both scenarios, with linked and unlinked intrinsic equivalent hydrogen column densities corresponding to the line-of-sight direction, $N_{\rm H,2}$, and the torus, $N_{\rm H}^{\rm torus}$, resulted in acceptable fits with C-statistic/degrees of freedom of 2308/2336 and 2301/2335, respectively. Neither the *Chandra* image nor the broadband X-ray spectrum provided evidence for the presence of an extended X-ray emission (Figure 2). We show the data, unfolded models, model components, and data-to-model ratios for the case of linked column densities in Figure 3. They are representative also of the unlinked column densities scenario.

We constrained the intrinsic photon index of the source, $\Gamma = 1.44^{+0.11}_{-0.01}$ and $\Gamma = 1.448^{+0.128}_{-0.002}$, for the linked and unlinked case, respectively (Table 2). We derived the absorbing column density of the torus and the line-of-sight column density: $N_{\rm H,2} = N_{\rm H}^{\rm torus}$ and $3.2^{+0.9}_{-0.4} \times 10^{23}\,{\rm cm}^{-2}$ (linked scenario), and $N_{\rm H}^{\rm torus} = 4.4^{+0.1}_{-0.2} \times 10^{23}\,{\rm cm}^{-2}$ and $1.3^{+0.9}_{-0.3} \times 10^{24}\,{\rm cm}^{-2}$ (unlinked scenario). This confirms the presence of a significant amount of cold matter surrounding OQ +208 with a large covering factor, CF > 0.5–0.6, that strongly attenuates the primary X-ray continuum. The torus column density of the unlinked scenario (porous torus) is ∼4 times higher than in the

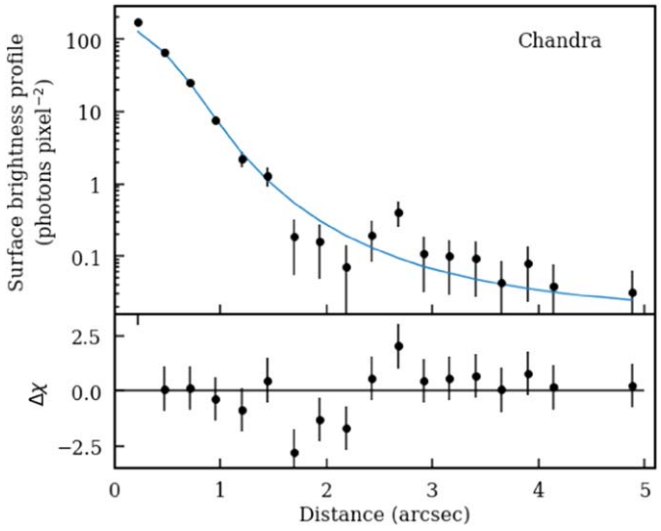

Figure 2. Top: surface brightness profile of OQ +208 resulting from the *Chandra* image. The solid line shows the model of the *Chandra* point-spread function corresponding to a point source. Bottom: model residuals of the fit. No evidence for an extended X-ray emission is detected.

linked scenario and is high enough to classify this source as a Compton thick AGN. Additionally, the data require an intrinsic absorbing column of the order of $N_{\rm H,1} \simeq 7 \times 10^{20}\,{\rm cm}^{-2}$ attributable to the host galaxy.

We find evidence for a strong fluorescent Fe emission around 6 keV (observer's frame). With the iron abundance of the torus fixed at the solar value and $C_{\rm line} = 1$, our spectral model appeared to underestimate the strength of the Fe–Kα line emission. Thus, we allowed $C_{\rm line}$ to vary and derived $C_{\rm line} = 3.5^{+0.4}_{-0.4}$ and $8.9^{+8.9}_{-2.5}$ for the linked and unlinked scenarios, respectively. Alternatively, we were able to obtain fits of comparable quality by keeping $C_{\rm line} = 1$ and by varying the iron abundance of the torus, which resulted in an abundance of ∼3 and ∼9 times the solar value for our two cases, accordingly. Allowing the normalization of the line component to vary does not affect the derived values for the column densities.

The soft part of the observed spectrum, between 0.5 and 4 keV, is dominated by scattered power-law emission with a relatively high scattering fraction of $C_{\rm scat} \simeq 0.6$–0.7.

Our modeling gives the rest-frame 0.5–30 keV de-absorbed luminosity of OQ +208 of the order of $10^{43}\,{\rm erg\,s^{-1}}$. Table 2 shows the contributions to this luminosity from the soft (0.5–2 keV), intermediate (2–10 keV), and hard (10–30 keV) X-ray bands. We also list the observed fluxes (not corrected for absorption) in these three energy bands (in the observed frame).

3.3. X-Ray Variability

We found that the *Chandra* and *XMM-Newton* PN cross-normalization constants are consistent with each other, indicating no flux variability between the 2003 and 2014 observations. However, the FPMA/B cross-normalization constants indicate that the normalization of the *NuSTAR* spectra is higher than that of the *Chandra* spectrum by up to ∼30%–40% over the 0.5–30 keV energy range used in the spectral fitting. According to Madsen et al. (2017), the *Chandra* calibration flux rises by up to 10%–15% above 4 keV compared to the *NuSTAR* flux. Thus, it is likely that the

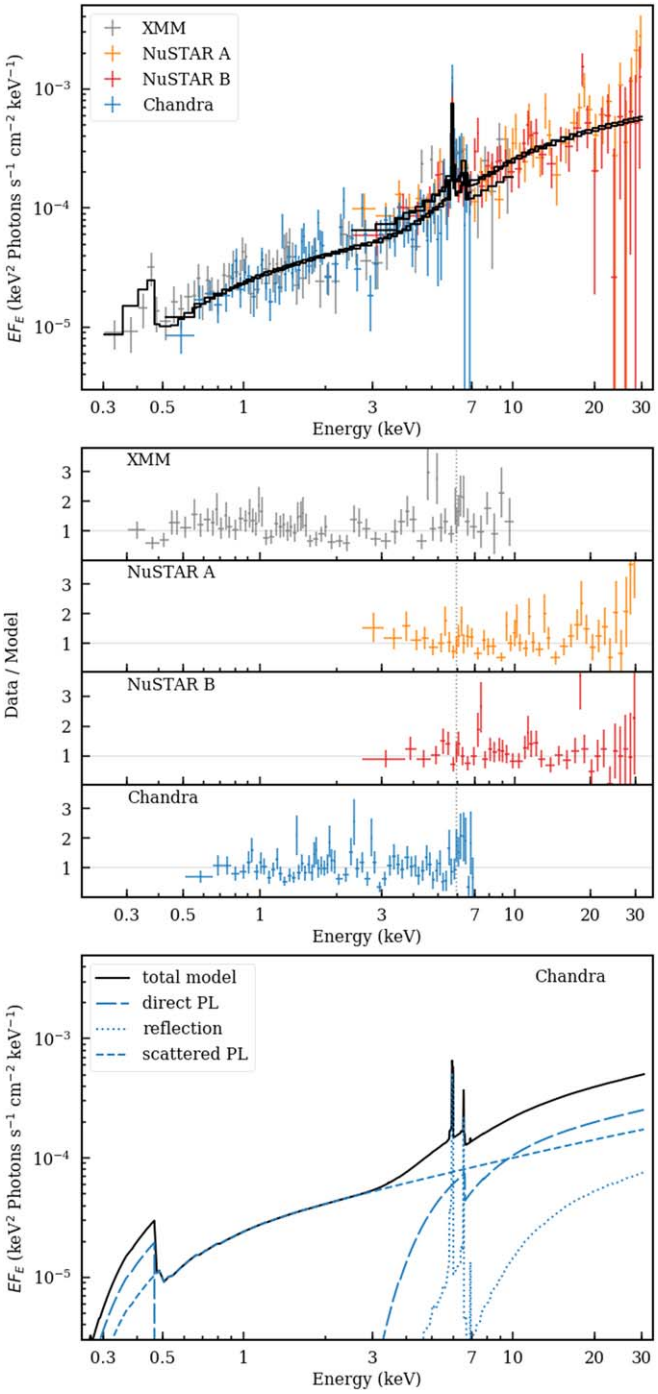

Figure 3. Top: unfolded data and models from the simultaneous fit of the new *Chandra* and *NuSTAR* data and archival *XMM-Newton* PN data sets in the scenario with the line-of-sight hydrogen and torus hydrogen column densities linked to each other. The unlinked scenario results in a fit of comparable quality. Center: corresponding data-to-model ratios. The vertical dotted line indicates the rest-frame energy of the 6.4 keV Fe fluorescent emission line. Bottom: unfolded model (solid line) and model components (direct absorbed power law, long-dashed line; reflection from a cold matter including fluorescent Fe emission, dotted line; scattered power law, short-dashed line) computed over the 0.3–30 keV energy band based on the model that provided the best fit to the *Chandra* data.

Table 2
Spectral Model Parameters

#	Description	Symbol	Value[a]		Unit
			$N_{\rm H}$ Linked	$N_{\rm H}$ Unlinked	
	(1)	(2)	(3)	(4)	(5)
1	Redshift	z	0.0766	0.0766	
2	Inclination angle	i	85	85	deg
3	Galactic equivalent hydrogen column density	$N_{\rm H}^{\rm gal}$	1.4	1.4	10^{20} cm^{-2}
4	Equivalent hydrogen column density of the host galaxy	$N_{\rm H,1}$	$6.8^{+1.3}_{-0.6}$	$6.6^{+0.03}_{-0.03}$	10^{20} cm^{-2}
5	Intrinsic line-of-sight equivalent hydrogen column density	$N_{\rm H,2}$	$0.44^{+0.01}_{-0.02}$	$0.32^{+0.09}_{-0.04}$	10^{24} cm^{-2}
6	Photon index of the direct emission	Γ	$1.45^{+0.11}_{-0.01}$	$1.448^{+0.128}_{-0.002}$	
7	Cutoff energy of the direct emission	$E_{\rm cut}$	300	300	keV
8	Equivalent hydrogen column density of the torus	$N_{\rm H}^{\rm torus}$	$N_{\rm H,2}$	$1.3^{+0.9}_{-0.3}$	10^{24} cm^{-2}
9	Covering factor of the torus	CF	$0.91^{+0.09}_{-0.32}$	$0.91^{+0.09}_{-0.44}$	
10	Constant normalizing the line emission component	$C_{\rm line}$	$3.5^{+0.4}_{-0.4}$	$8.9^{+8.9}_{-2.5}$	
11	Iron abundance of the torus	$A_{\rm Fe}$	1	1	Solar
12	Scattering fraction of the direct power law	$C_{\rm scat}$	$0.61^{+0.05}_{-0.14}$	$0.69^{+0.06}_{-0.18}$	
13	Cross-normalization constant	$A_{\rm chandra}$	1	1	
14	Cross-normalization constant	$A_{\rm xmm}$	$1.05^{+0.03}_{-0.04}$	$1.09^{+0.04}_{-0.03}$	
15	Cross-normalization constant	$A_{\rm nA}$	$1.36^{+0.02}_{-0.05}$	$1.38^{+0.18}_{-0.07}$	
16	Cross-normalization constant	$A_{\rm nB}$	$1.28^{+0.07}_{-0.19}$	$1.30^{+0.11}_{-0.02}$	
17	Soft 0.5–2 keV observed frame flux[b]	$F_{\rm soft}$	0.61 ± 0.08	0.62 ± 0.08	10^{-13} erg cm^{-2} s^{-1}
18	Intermediate 2–10 keV observed frame flux[b]	$F_{\rm intm}$	2.9 ± 0.4	3.1 ± 0.4	10^{-13} erg cm^{-2} s^{-1}
19	Hard 10–30 keV observed frame flux[b]	$F_{\rm hard}$	6.5 ± 0.8	7.1 ± 1.0	10^{-13} erg cm^{-2} s^{-1}
20	Soft 0.5–2 keV rest-frame intrinsic luminosity[b]	$L_{\rm soft}$	1.7 ± 0.2	1.5 ± 0.2	10^{42} erg s^{-1}
21	Intermediate 2–10 keV rest-frame intrinsic luminosity[b]	$L_{\rm intm}$	4.5 ± 0.6	4.0 ± 0.6	10^{42} erg s^{-1}
22	Hard 10–30 keV rest-frame intrinsic luminosity[b]	$L_{\rm hard}$	6.1 ± 0.8	5.5 ± 0.7	10^{42} erg s^{-1}
	C-statistic		2308	2301	
	Degrees of freedom		2336	2335	

Notes.
[a] Columns (1) and (2) provide the description of the model parameters. Columns (3) and (4) give model parameter values for the two scenarios, with $N_{\rm H,2}$ and $N_{\rm H}^{\rm torus}$ linked to each other and unlinked, respectively. Column (5) gives the units of the model parameters.
[b] Mean and standard deviation of the 68% confidence level measurements from the four individual data sets.

X-ray flux of OQ +208 varied between 2014 and 2016 by up to ∼50%.

4. Discussion

Young radio sources have been proposed to be X-ray and γ-ray emitters based on theoretical considerations in which their high-energy emission originates due to the inverse Compton scattering of ambient soft photon fields off energetic electrons injected into expanding lobes from the hot spots (e.g., Stawarz et al. 2008; Ostorero et al. 2010). A small sample of 16 CSOs have been observed and detected in the soft X-rays with *Chandra* and/or *XMM-Newton* (S16 and references therein), and Migliori et al. (2016) reported the detection of PKS 1718 + 654 in the γ-ray band with *Fermi*Large Area Telescope. Here, we presented new *Chandra* and *NuSTAR* observations of the young radio source OQ +208. The source was clearly detected with both instruments. The *NuSTAR* detection constitutes the first hard X-ray (>10 keV) detection of a CSO and establishes CSOs as a new class of *NuSTAR* sources. We modeled the *NuSTAR* and *Chandra* data simultaneously, also including the archival *XMM-Newton* PN data set, assuming a model in which the direct power-law X-ray emission interacts with the obscuring cold matter surrounding the central black hole through absorption, reflection, and scattering processes (Baloković et al. 2018).

4.1. Origin of the X-Ray Emission

The broadband X-ray coverage of our observations enabled us to constrain the photon index of the primary X-ray emission from the source and to measure the 0.5–30 keV (rest-frame) intrinsic luminosity of $L_{\rm X} \sim 10^{43}$ erg s^{-1}. The photon index of $\Gamma \simeq 1.45$ is relatively hard compared to the photon indexes derived for *XMM-Newton*- and *NuSTAR*-detected AGN (e.g., Corral et al. 2011; Del Moro et al. 2017). It is, however, rather typical of the X-ray spectra from accreting black hole binaries in a hard jet-producing spectral state (e.g., Remillard & McClintock 2006; Done et al. 2007). Power-law X-ray emission with such a photon index could be produced e.g., in an accretion disk corona, expanding radio lobes, or relativistic jets. However, the observed level of X-ray emission is lower than the level of X-ray emission due to the inverse Compton scattering of the infrared and ultraviolet photons off ultra-relativistic electrons in the radio lobes expected for this source (Ostorero et al. 2010, Figure 1, Appendix A.9). This could indicate that in the young radio lobes of OQ +208, the magnetic pressure dominates over the electron pressure rather than remaining in rough equipartition with them, as assumed in Stawarz et al. (2008). Detailed modeling of the broadband radio-to-hard-X-ray spectral energy distribution is beyond the scope of this work and will be addressed in a forthcoming work.

Nonetheless, the bolometric luminosity of the source derived in A. Wójtowicz et al. (2019, in preparation) using the Richards et al. (2006) bolometric correction applied to the observed 12 μm luminosity (E. Kosmaczewski et al., in preparation) yields $L_{\rm bol} \simeq 4.3 \times 10^{45}\,{\rm erg\,s^{-1}}$. For the black hole mass of $M_{\rm BH} = 5 \times 10^8\ M_\odot$ (Wu 2009) and $L_{\rm Edd} = 1.3 \times 10^{38}\,(M_{\rm BH}/M_\odot)$, this bolometric luminosity corresponds to the Eddington luminosity ratio of $\lambda_{\rm Edd} = L_{\rm bol}/L_{\rm Edd} \simeq 0.06$. However, the 2–10 keV X-ray luminosity expected from a radio-loud AGN with a similar bolometric luminosity is of the order of $(3\text{–}7) \times 10^{43}\,{\rm erg\,s^{-1}}$, based on the bolometric corrections obtained by Runnoe et al. (2012), i.e., an order of magnitude higher than the 2–10 keV luminosity resulting from our modeling of the X-ray spectrum of OQ +208 (see Table 2). It is thus possible that the X-ray radiation mechanism of OQ +208 is less efficient than that of the quasars used by Runnoe et al. to derive the bolometric corrections or the bolometric luminosity based on the 12 μm luminosity is overestimated.

4.2. Properties of the X-Ray Absorber

Our observations allowed us to gain important insights into the nature of the intrinsic obscuration in OQ +208. We adopted the torus model of Baloković et al. (2018) and detected intrinsic absorption with the equivalent hydrogen column density of the order of 10^{23}–$10^{24}\,{\rm cm^{-2}}$ due to cold matter surrounding the central black hole with a large covering factor. It seems plausible that the torus has a porous structure, given the good fit to the data of the model with the line-of-sight absorbing column and torus absorbing column varying freely and resulting in values that are statistically different from each other. This conclusion is further supported by the detection of a significant amount of the scattered primary emission dominating the soft X-ray spectrum below 4 keV. With a porous structure, the primary emission would undergo less attenuation as it could arrive to the observer through the holes in the torus. The optical classification as a broad-line quasar is also consistent with the porous structure of the torus obscuring an X-ray source seen from a direction typical to Type 2 quasars. Additionally, a variable degree of the porosity of the obscurer could explain the ∼50% X-ray flux variability that the source appeared to undergo between our *Chandra* and *NuSTAR* observations.

Alternatively, OQ +208 could belong to the so-called type-12 AGN class, which is optically unobscured but X-ray obscured, in which the X-ray obscuration was argued to be produced by dust-free gas within (or inside) the broad-line region (e.g., Merloni et al. 2014, and references therein). However, it was shown that majority of such AGNs tend to have rather high X-ray luminosities compared to OQ +208 (e.g., Merloni et al. 2014; Marchesi et al. 2016).

When modeling only the *XMM-Newton* data, Guainazzi et al. (2004) found that the emission feature around 6 keV (the observer's frame) can be modeled either as a single broad line with energy corresponding to the neutral Fe or by a combination of three narrow lines, whose energies are consistent with neutral, He-like, and H-like Fe. Our modeling corresponds to the latter scenario (Baloković et al. 2018).

Moreover, we observed that the fluorescent iron line emission was enhanced relative to the strength of the associated Compton reflection continuum. This may indicate a significant departure of the Fe–K reflection region from the structure of our model or could alternatively suggest an elevated iron abundance in the matter forming the torus. Importantly, 6.4 keV line emission from an extended hundred pc-scale region has been resolved in a few nearby galaxies (e.g., Fabbiano et al. 2018, 2019). Additionally, an enhanced line emission with spatially variable equivalent width has been reported by Marinucci et al. (2017). The spatial scales studied by these authors cannot be resolved in X-rays in our source nor is the possible extended 6.4 keV emission accounted for by the existing torus models.

We did not find evidence for a diffuse X-ray component in OQ +208, contrary to the work of Lanz et al. (2016) based on the *Chandra* data alone. In fact, the combined *Chandra*, *XMM-Newton*, and *NuSTAR* observations show that their model (two thermal components and an absorbed power law) cannot account for the 6–7 keV Fe emission signature and the overall shape of the hard X-ray spectrum.

5. Conclusions

Our results indicate that in OQ +208, the young ∼250 yr old radio lobes spanning the length of 10 pc coexist with a cold obscuring matter, possibly a dusty torus. The structure of the torus is likely porous, with a highly equivalent column density comparable to that detected in Compton thick AGNs. The X-ray source is powered by accretion with a relatively high Eddington ratio of $\lambda_{\rm Edd} \sim 0.06$ and emits a rather hard power-law spectrum, which might have increased in the flux by ∼50% between our 2014 and 2016 observations. The X-ray emission is consistent with a point source based on the *Chandra* image, and it is not likely to originate from the young radio lobes, unless the lobes in OQ +208 are dominated by the magnetic pressure.

This research has made use of data obtained by the *Chandra* X-ray Observatory and software provided by the *Chandra* X-ray Center (CXC). It made also use of data from the *NuSTAR* mission, a project led by the California Institute of Technology, managed by the Jet Propulsion Laboratory, and funded by the National Aeronautics and Space Administration. This research has made use of the *NuSTAR* Data Analysis Software (NuSTARDAS) jointly developed by the ASI Science Data Center (ASDC, Italy) and the California Institute of Technology (USA). This project was supported in part by the NASA grants GO4-15099X and NNX17AC23G. M.S. and A.S. were supported by NASA contract NAS8-03060 (Chandra X-ray Center). M.S. acknowledges the Polish NCN grant OPUS 2014/13/B/ST9/00570. L.S. was supported by Polish NSC grant 2016/22/E/ST9/00061.

ORCID iDs

Małgosia Sobolewska https://orcid.org/0000-0002-6286-0159
Aneta Siemiginowska https://orcid.org/0000-0002-0905-7375
Giulia Migliori https://orcid.org/0000-0003-0216-8053
Luisa Ostorero https://orcid.org/0000-0003-3983-5980
Łukasz Stawarz https://orcid.org/0000-0001-8294-9479

References

Arnaud, K. A. 1996, in ASP Conf. Ser. 101, Astronomical Data Analysis Software and Systems V, ed. G. Jacoby & J. Barnes (San Francisco, CA: ASP), 17

Astropy Collaboration, Price-Whelan, A. M., Sipőcz, B. M., et al. 2018, AJ, 156, 123
Baloković, M., Brightman, M., Harrison, F. A., et al. 2018, ApJ, 854, 42
Begelman, M. C., & Cioffi, D. F. 1989, ApJL, 345, L21
Corral, A., Della Ceca, R., Caccianiga, A., et al. 2011, A&A, 530, A42
Del Moro, A., Alexander, D. M., Aird, J. A., et al. 2017, ApJ, 849, 57
Done, C., Gierliński, M., & Kubota, A. 2007, A&ARv, 15, 1
Fabbiano, G., Paggi, A., Siemiginowska, A., et al. 2018, ApJL, 869, L36
Fabbiano, G., Siemiginowska, A., Paggi, A., et al. 2019, ApJ, 870, 69
Fruscione, A., et al. 2006, Proc. SPIE, 6270, 60
Guainazzi, M., Siemiginowska, A., Rodriguez-Pascual, P., & Stanghellini, C. 2004, A&A, 421, 461
Harrison, F. A., Craig, W. W., Christensen, F. E., et al. 2013, ApJ, 770, 103
Heinz, S., Reynolds, C. S., & Begelman, M. C. 1998, ApJ, 501, 126
Hinshaw, G., Larson, D., Komatsu, E., et al. 2013, ApJS, 208, 19
Lanz, L., Ogle, P. M., Alatalo, K., & Appleton, P. N. 2016, ApJ, 826, 29
Madsen, K. K., Beardmore, A. P., Forster, K., et al. 2017, AJ, 153, 2
Marchesi, S., Lanzuisi, G., Civano, F., et al. 2016, ApJ, 830, 100
Marinucci, A., Bianchi, S., Fabbiano, G., et al. 2017, MNRAS, 470, 4039
Marziani, P., Sulentic, J. W., Calvani, M., et al. 1993, ApJ, 410, 56
Merloni, A., Bongiorno, A., Brusa, M., et al. 2014, MNRAS, 437, 3550
Migliori, G., Siemiginowska, A., Kelly, B. C., et al. 2014, ApJ, 780, 165
Migliori, G., Siemiginowska, A., Sobolewska, M., et al. 2016, ApJL, 821, L31
Ostorero, L., Moderski, R., Stawarz, Ł., et al. 2010, ApJ, 715, 1071
Remillard, R. A., & McClintock, J. E. 2006, ARA&A, 44, 49
Reynolds, C. S., Heinz, S., & Begelman, M. C. 2001, ApJL, 549, L179
Richards, G. .T, Lacy, M., Storrie-Lombardi, L. J., et al. 2006, ApJS, 166, 470
Runnoe, J. C., Brotherton, M. S., & Shang, Z. 2012, MNRAS, 426, 2677
Siemiginowska, A. 2009, AN, 330, 264
Siemiginowska, A., LaMassa, S., Aldcroft, T. L., Bechtold, J., & Elvis, M. 2008, ApJ, 684, 811
Siemiginowska, A., Sobolewska, M., Migliori, G., et al. 2016, ApJ, 823, 57
Sobolewska, M., Siemiginowska, A., Guainazzi, M., et al. 2019, ApJ, 871, 71
Stanghellini, C., O'Dea, C. P., Baum, S. A., & Laurikainen, E. 1993, ApJS, 88, 1
Stanghellini, C., O'Dea, C. P., Baum, S. A., et al. 1997, A&A, 325, 943
Stawarz, Ł., Ostorero, L., Begelman, M. C., et al. 2008, ApJ, 680, 911
Tengstrand, O., Guainazzi, M., Siemiginowska, A., et al. 2009, A&A, 501, 89
Wagner, A. Y., & Bicknell, G. V. 2011, ApJ, 728, 29
Wu, F., An, T., Baan, W. A., et al. 2013, A&A, 550, A113
Wu, Q. W. 2009, ApJL, 701, L95
Yaqoob, T. 2012, MNRAS, 423, 3360